Probing Glass Formation in Perylene Derivatives via Atomic Scale Simulations and Bayesian Regression

Eric Lindgren,[1] Jan Swenson,[1] Christian Müller,[2] and Paul Erhart[1,*]

[1] *Department of Physics, Chalmers University of Technology, SE-41296, Gothenburg, Sweden*
[2] *Department of Chemistry and Chemical Engineering, Chalmers University of Technology, SE-41296, Gothenburg, Sweden*

While the structural dynamics of chromophores are of interest for a range of applications, it is experimentally very challenging to resolve the underlying microscopic mechanisms. Glassy dynamics are also challenging for atomistic simulations due to the underlying dramatic slowdown over many orders of magnitude. Here, we address this issue by combining atomic scale simulations with autocorrelation function analysis and Bayesian regression, and apply this approach to a set of perylene derivatives as prototypical chromophores. The predicted glass transition temperatures and kinetic fragilities are in semi-quantitative agreement with experimental data. By analyzing the underlying dynamics via the normal vector autocorrelation function, we are able to connect the β and α-relaxation processes in these materials to caged (or librational) dynamics and cooperative rotations of the molecules, respectively. The workflow presented in this work serves as a stepping stone toward understanding glassy dynamics in many-component mixtures of perylene derivatives and is readily extendable to other systems of chromophores.

Chromophores are an important class of materials with a range of potential and realized applications in the area of energy conversion thanks to their exceptional optical properties. Chromophores have been studied, e.g., as active materials in solar cells [1–5], organic light-emitting diodes [6, 7], and photoswitchable and solar thermal storage systems [8–10]. The properties of these materials are sensitive to both the structural arrangements of the molecules and their dynamic behavior. The dynamics as manifested in macroscopic properties such as viscosity and diffusivity, are also important for solution processing, which is currently the most common approach for large-scale manufacturing of devices based on these materials. Controlling viscosity and diffusivity is often achieved through glass formation [11], which can occur upon rapid cooling, bypassing crystallization and resulting in a glassy state that lacks long-range order. The glass transition is characterized by a dramatic slow down in the materials dynamics over a narrow temperature range that is commonly probed via the temperature dependence of, e.g., the viscosity (via rheometry), the density (via dilatometry) or the heat exchanged with the environment (via calorimetry).

For practical use, it is crucial to achieve glass formation controllably at modest cooling rates. In this context, using mixtures of perylene derivatives, it has been shown that increasingly stronger glass formers can be systematically obtained by increasing the number of components. This principle works even though the underlying molecules are weak ("fragile") glass formers in single-component systems [12]. Moreover, it has been found that such many-component mixtures have further benefits, including significantly improved thermal stability [13]. While many-components mixtures thus have very high potential for materials design, the much larger design space also renders understanding the underlying dynamical processes much more challenging. Here, as a first step toward a systematic understanding of these materials, we investigate glass formation in *single*-component liquids of perylene derivatives (Fig. 1a) using molecular dynamics (MD) simulations in combination with Bayesian regression.

While the microscopic dynamics of glass-forming systems can be explored via MD simulations [14, 15], it is usually impossible to directly access the temperature range in which the glass transition occurs due the timescale limitations of this technique. Here, to extend the temperature range, we combine MD simulations with Bayesian regression, which allows us to predict glass transition temperatures as well as the propensity for glass formation (expressed via the kinetic fragility). To this end, we observe the temperature dependence of the dynamics via the diffusivity, which is anticorrelated with the viscosity but computationally easier to converge than the latter. Our results for the glass transition temperatures and the kinetic fragility are in semi-quantitative agreement with experimental data, supporting the viability of the simulation approach. To gain insight into the microscopic processes we analyze the time-autocorrelation function (ACF) of the molecular orientation, which reveals three distinct dynamic regimes corresponding to intramolecular motion as well as β and α-relaxation processes. Our work thereby establishes the viability of this simulation approach and lays the groundwork for future studies of the evolution of the dynamics in many-component mixtures.

We considered five perylene derivatives (Fig. 1a), which differ with respect to the length n of the pendant alkyl chain C_nH_{2n+1} attached to one of the bay positions. Monomer **I** corresponds to regular perylene with no alkyl chain, whereas monomers **II**–**V** have alkyl chains containing two ($n = 2$), four ($n = 4$), six ($n = 6$), and twelve ($n = 12$) carbon atoms, respectively.

To characterize the dynamics of the perylene deriva-

* erhart@chalmers.se

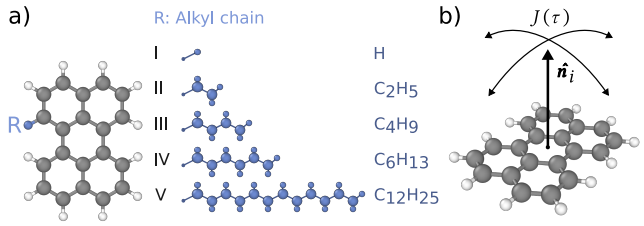

FIG. 1. (a) Perylene derivatives studied in this work. (b) Schematic representation of the normal vector autocorrelation function $J(\tau)$, see Eq. 2.

tives, we first consider the molecular diffusivity D, which can be obtained from the MSD $\langle \Delta r^2 \rangle$ of the molecular centroid positions [16],

$$\langle \Delta r^2 \rangle = 6D\tau \tag{1}$$

The diffusivity was computed using production runs with a duration of up to 10 ns.

To obtain more detailed insight into the underlying microscopic properties, we also analyzed the ACF of the normal vectors indicating the orientation of each individual molecule (Fig. 1b) given by

$$J(\tau) = \langle \hat{\boldsymbol{n}}_i(t) \cdot \hat{\boldsymbol{n}}_i(t+\tau) \rangle_{it} \tag{2}$$

Here, $\hat{\boldsymbol{n}}_i(t)$ is the normal vector of molecule i (Sect. S1). The ensemble average applies over all times t and each molecule i in the system. Equation (2) can be efficiently evaluated using the Wiener-Kinchin theorem.

One may also extract the standard error as an uncertainty estimate for $J(\tau)$ from the ACF for each molecule $J_i(\tau)$ before computing the ensemble average in Eq. 2 according to

$$\sigma_J(\tau) = \sqrt{\mathrm{Var}\left(\{J_i\}_{i=1}^N\right) \Big/ N}, \tag{3}$$

where N is the number of molecules in the system.

Since the ACFs spans multiple orders of magnitude in time, production runs of different length were conducted. To sample short and long-time scales, simulations with a length of respectively 100 ps and 10 ns were carried out with snapshots being written every 1 fs and 100 fs, respectively (Sect. S1). The normal vector ACFs were calculated for both production runs and subsequently spliced together at a time lag of 1 ps.

We begin by analyzing the temperature dependence of the molecular diffusivity (Fig. 2a; also see Sect. S2). When obtaining these data from MD simulations we are limited by the time scale that is reachable via the latter. While one can reach on the order of 1 µs in total simulation length, one has to keep in mind that computing the diffusivity via the MSD according to Eq. 1 requires oversampling. For the present systems, this implies that the MSD can no longer be reliably obtained for temperatures below approximately 400 K. This is below the experimental melting point of pure perylene of around 550 K but above the experimental glass transition temperatures, which range around 250 K [12].

In order to be able to gain information about the behavior at these temperatures, we need to extrapolate. However, since the diffusivity and other properties change rapidly over many orders of magnitude in this region, this extrapolation must be done with care and account for error propagation. To this end, we employ the VFT equation and combine it with Bayesian regression. The former describes the temperature dependence of, e.g., the viscosity or the diffusivity of fragile glass formers, allowing for non-Arrhenius behavior. While the VFT equation is empirical in nature, it is widely used in the analysis of glass-forming systems and provides an accurate fit for many experimental observations as well as the data obtained here (Fig. 2a). For the diffusivity it reads

$$D(T) = D_0 \exp\left[-B/\left(T - T_{\mathrm{VF}}\right)\right], \tag{4}$$

where D_0 is a prefactor, T_{VF} is the Vogel-Fulcher temperature, and B is a parameter akin to a pseudo-activation energy [17]. The parameters of the VFT equation can in turn be used to compute the kinetic fragility $m = B\,T_g/\left[\ln(10)\cdot(T_g - T_{\mathrm{VF}})^2\right)\big]$, where T_g is the estimated glass transition temperature [18, 19].

Due to the exponential in Eq. 4 extrapolation and error propagation require care, which we handle here via Bayesian regression. The latter is a technique in which a model $M(\boldsymbol{\theta})$ with parameters represented by a parameter vector $\boldsymbol{\theta} = [D_0, T_{\mathrm{VF}}, B]$ is fitted to a set of data $\mathcal{D}$ given prior information $\mathcal{I}$, using Bayes' theorem,

$$p(\boldsymbol{\theta}|\mathcal{D},\mathcal{I}) \propto p(\mathcal{D}|\boldsymbol{\theta},\mathcal{I})p(\boldsymbol{\theta}|\mathcal{I}) \tag{5}$$

The advantage of a Bayesian approach is twofold. First, prior beliefs are clearly stated in the prior distribution $p(\boldsymbol{\theta}|\mathcal{I})$. Second, error estimates are readily extractable from the posterior distribution $p(\boldsymbol{\theta}|\mathcal{D},\mathcal{I})$, since data uncertainties and errors can be encoded in the likelihood function $p(\mathcal{D}|\boldsymbol{\theta},\mathcal{I})$. We then sample the posterior distribution $p(\boldsymbol{\theta}|\mathcal{D},\mathcal{I})$ via Markov-chain Monte Carlo (MCMC) simulations using the diffusivity data from MD simulations to fit the VFT equation (see Sect. S3 for details). This allows us to extrapolate the diffusivity to lower temperatures along with controlled error estimates (Fig. 2a).

The temperature at which the system transitions into a glassy state is denoted by the glass transition temperature T_g. T_g cannot be uniquely defined but is rather set by a pragmatic property-dependent threshold. For example, one often takes T_g as the temperature where the viscosity reaches a value of $10^{11}\,\mathrm{Pa}\cdot\mathrm{s}$ [19]. In the present work, when considering the diffusivity, we adopt a threshold of $17 \times 10^{-22}\,\mathrm{m}^2/\mathrm{s}$, which corresponds to a MSD of $100\,\mathrm{Å}^2$ over 100 s. In other words, it specifies the onset of diffusion beyond the first-nearest neighbor

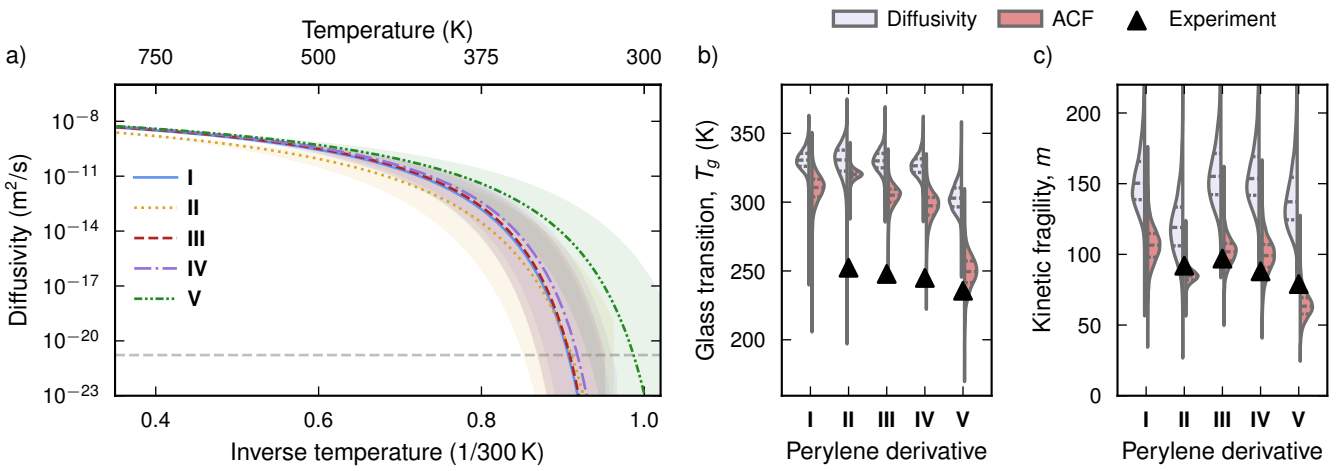

FIG. 2. (a) Extrapolation of the temperature dependence of the VFT fit of the diffusivity to lower temperatures (see Sect. S2 in the Supplementary Information for the MD data). The glass transition temperature T_g is defined as the temperature where the MSD over 100 s reaches 100 Å, denoted by the horizontal gray dashed line. The error band corresponds to one standard deviation. (b,c) Violin plots of (b) the glass transition temperature T_g and (c) the kinetic fragility m estimated from both the diffusivity and the normal vector ACF. Experimental values are from Ref. 12. T_g values were experimentally obtained from DSC first heating thermograms with a heating rate of $0.17\,\mathrm{K}\cdot\mathrm{s}^{-1}$. The kinetic fragility was obtained from FSC measurements for various cooling rates as $m = -d\log|q|/d(T_g/T_f')|_{T_f'=T_g}$, where q is the cooling rate and T_f' is the fictive FSC temperature. The simulated values for the kinetic fragility were computed from the VFT parameters as $m = B\,T_g/\left[\ln(10)\cdot(T_g - T_{\mathrm{VF}})^2)\right]$. Note that T_g is typically not observed experimentally for derivative **I**, due to its strong tendency to crystallize.

shell. We emphasize that since the viscosity and similarly the diffusivity change very steeply around the glass transition (Fig. 2a) the threshold value has only a modest effect on the values obtained for T_g. For example, increasing or decreasing the threshold by two orders of magnitude changes our estimates for T_g by only $\pm 5\,\mathrm{K}$

The glass transition temperatures obtained here are in semi-quantitative agreement with experiments, and correctly predict the trend from **II** to **V** [12] (Fig. 2b). However, the simulated T_g values are overestimated compared to experimental values obtained by differential scanning calorimetry (DSC) by 50 K to 70 K. The predicted kinetic fragilities are also in agreement with experimentally obtained values from fast scanning calorimetry (FSC) (Fig. 2c).

The glass transition temperature decreases systematically with increasing alkyl chain length. Conceptually, this can be explained by an increase in the effective volume available to each molecule caged by its neighbors, due to the longer pendant groups. It is, however, noteworthy that the kinetic fragility exhibits a maximum for **III**, which features a butyl pendant chain — a non-trivial behavior that is observed in both experiment and simulation.

We now turn to the normal vector ACF $J(\tau)$ (Eq. 2) to gain further insight into the relaxation processes close to the glass transition (Fig. 3a). We demonstrate the procedure for obtaining the temperature dependence of $J(\tau)$ for derivative **I**, noting that the general temperature dependence of $J(\tau)$ is consistent for all perylene derivatives **I**–**V** (see Supplementary Information Sect. S4 for the ACFs for all perylene derivatives).

First, we observe that the correlation time of $J(\tau)$ depends strongly on temperature, ranging from 100 ps at 800 K to $>$ 10 ns at 400 K. At 800 K the perylene molecules thus maintain their orientation over a time scale on the order of 100 ps, while they are effectively locked in their orientation over 10 ns at 400 K.

Second, the ACFs can be described by the sum of two exponential functions and one stretched exponential function, where the latter is a common feature of correlation functions in glassy systems [20]

$$J(\tau) = A_1 e^{-\tau/\tau_1} + A_2 e^{-\tau/\tau_2} + (1 - A_1 - A_2) e^{(-\tau/\tau_3)^\beta} \quad (6)$$

The timescales τ_1, τ_2, and τ_3 are separated by several orders of magnitude at low temperatures, with $\tau_1 \approx 0.1$ ps, $\tau_2 \approx 10$ ps, and $\tau_3 \approx 1$ ns at 450 K. $\beta \leq 1$ is the stretch exponent for the long timescale component.

We can apply the same Bayesian regression workflow as for the diffusivity to estimate the glass transition temperature and kinetic fragility from the temperature dependence of the normal vector ACF. However, an additional step is required compared to the diffusivity, as the normal vector ACF needs to be fitted to Eq. 6 for each temperature (Fig. 3b). Each fit yields a full posterior probability distribution $p(A_1, A_2, \tau_1, \tau_2, \tau_3, \beta | T, \mathcal{D}, \mathcal{I})$. An estimate for the timescale of the slowest process captured by the ACF presented by τ_3 with uncertainty estimates can then be obtained from the marginal distribution $p(\tau_3 | T, \mathcal{D}, \mathcal{I})$ for each temperature (Fig. 3c). A VFT equation of the

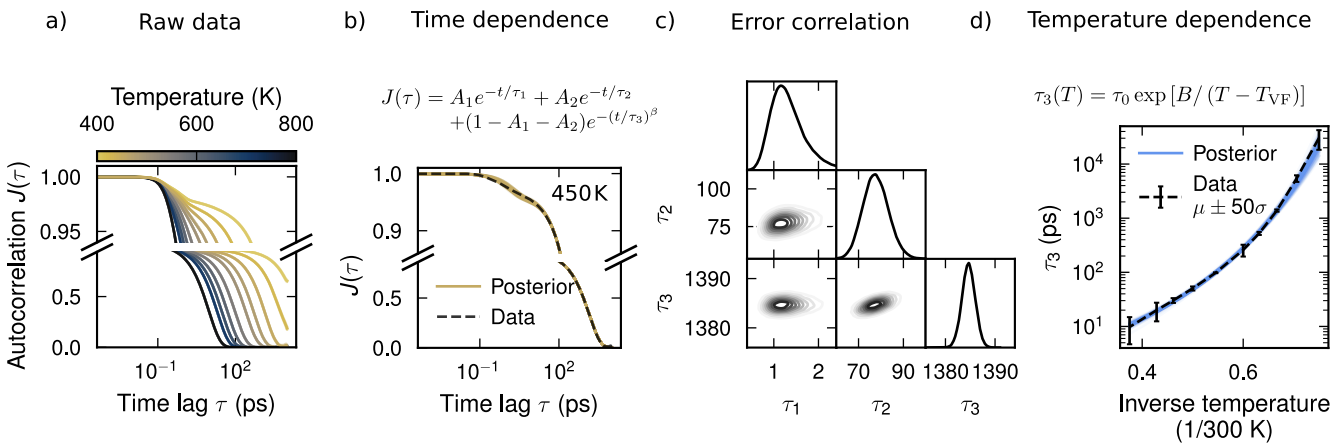

FIG. 3. Bayesian regression workflow used to extrapolate the normal vector ACF to longer timescales. (a) Normal vector ACFs for perylene derivative **I** at different temperatures. Note that the y-axis has been split using different scales to reveal the multiple steps in the ACF. (b) Normal vector ACF for perylene derivative **I** at 45 K along with the corresponding posterior distribution of fits to Eq. 6. (c) Subset of the posterior distribution in (b), $p(\tau_1, \tau_2, \tau_3|\mathcal{D}, \mathcal{I})$, shown as a corner plot. (d) Fit to the VFT expression Eq. 7 using the mean μ, and standard deviation σ of the marginal distribution $p(\tau_3|\mathcal{D}, \mathcal{I})$.

form

$$\tau_3(T) = \tau_0 \exp\left[B/\left(T - T_{\mathrm{VF}}\right)\right], \tag{7}$$

is then fitted to the temperature dependence of τ_3, which allows for a similar extrapolation to longer timescales as in the case of the diffusivity (Fig. 4). Here, the threshold for τ_3 above which the system is deemed to be in a glassy state was again taken to be 100 s [19]. Note that the resulting glass transition temperature is relatively insensitive to this particular threshold, as increasing or decreasing the threshold by two orders of magnitude only changes T_g by ± 7 K.

The estimates for both the glass transition temperature and the kinetic fragility from the normal-vector ACF and the diffusivity generally agree with each other (Fig. 2b,c). Both schemes capture the trend of decreasing T_g with increasing length of the alkyl chain of the perylene derivative. However, the estimates from the diffusivity are higher than those from the normal-vector ACF typically by 10 K to 30 K for the glass transition temperature and by 10 to 40 for the kinetic fragility. This difference is due to the two observables probing different processes. The diffusivity is sensitive to the diffusion of the monomers, while the normal vector ACF probes the rotational motion of the monomer. The normal vector ACF and the diffusivity are thus complementary. The difference in T_g between both observables suggests that the monomers continue to rotate on long timescales 10 K to 30 K below the temperature at which diffusion has slowed down.

We can elucidate the relaxation processes in the system by decomposing the ACF into the contribution of each exponential function that make up $J(\tau)$ (Fig. 5). The separation of timescales between the processes allows the selective application of frequency filters in the Fourier domain, corresponding to the timescales represented by τ_1, τ_2, and τ_3. These filters are applied to the trajectory of a single perylene molecule extracted from the entire MD trajectory, and allows us to single out the dynamics that correspond to each process (see the supplementary movie for a visual representation of this scheme, and Sect. S5 of the Supplementary Information for further details).

We study the dynamics of perylene derivative **I** at a temperature of 450 K as an example of this scheme (Fig. 5). The fastest process with time scale τ_1 corresponds to intramolecular atomic motion. The second fastest process, τ_2, corresponds to β-relaxation enforced by caging by neighboring molecules, such as libration and twisting of the perylene core. Neither the τ_1 nor the τ_2 processes significantly affect the orientation of the molecule, as is evident by their small amplitude. The bulk of the autocorrelation function $J(\tau)$ is made up of the slow τ_3 process. τ_3 corresponds to cooperative intermolecular processes, such as reorientation of molecules. The reorientation of a molecule requires neighboring molecules to rotate, which takes place over rapidly increasing timescales as the temperature is decreased. The experimental and simulated values of the kinetic fragility indicate that all derivatives studied in this work are fragile glass formers. In fragile glass formers, the level of cooperation decreases significantly at temperatures greater than T_g [21]. That τ_3 captures cooperative reorientation even in the supercooled regime at 450 K thus indicates that it is sensitive to processes that are more prominent close to the glass transition in fragile glass formers. Based on this, we attribute τ_3 to be related to α-relaxation, and that the microscopic mechanism driving glass formation in perylene derivatives **I**–**V** is the cooperative reorientation of the molecules.

Given the sources of uncertainty related to the under-

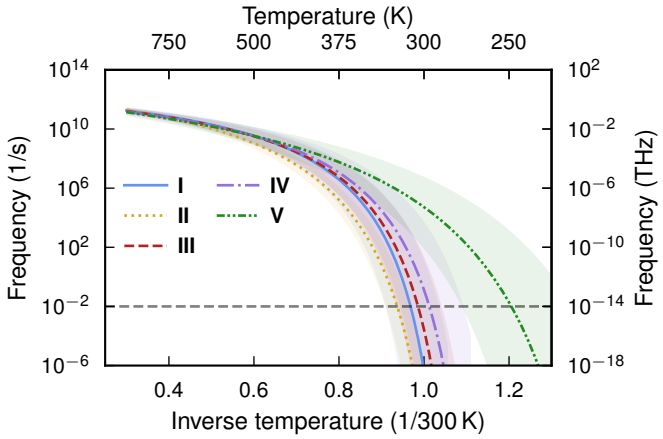

FIG. 4. Extrapolation of the temperature dependence of the slowest process represented by $\tau_3(T)$, to lower temperatures and thus lower frequencies. The error band corresponds to $\pm$ one standard deviation. T_g is defined to be the temperature which the timescale reaches 100 s, represented by the horizontal gray dashed line.

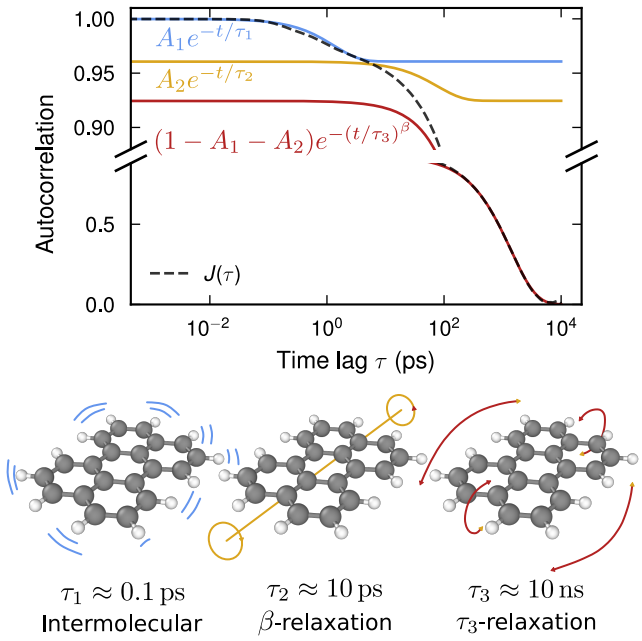

FIG. 5. Decomposition of the normal vector ACF $J(\tau)$ into individual exponential functions representing three different relaxation processes. The fastest process with a correlation time of about 0.1 ps at 450 K corresponds to intramolecular atomic motion. The second one (β-relaxation) with a correlation time of approximately 10 ps at 450 K corresponds to librational motion and twisting of the perylene core. Finally, the slowest process (τ_3-relaxation) with a correlation time of approximately 10 ns at 450 K corresponds to the hindered rotational reorientation of the perylene molecules due to intermolecular interactions.

lying empirical force field used in the MD simulations and the extrapolation over many orders of magnitude, we consider the overall agreement of the predicted glass transition temperatures and kinetic fragilities with the experimental data very encouraging. The normal vector ACF in particular show semi-quantiative agreement with experiments, with the ACF systematically yielding both lower glass transition temperatures and kinetic fragilities than the diffusivity (Fig. 2b,c). This difference highlights the complementarity of the diffusivity and the normal vector ACF, as they are more sensitive to molecular diffusion and rotation, respectively. The estimated higher value of the glass transition temperature from the diffusivity can be understood as molecular diffusion freezing in at a higher temperature compared to rotation. The processes driving glass formation are thus cooperative rotational processes, as elucidated by the decomposition of the normal vector ACF. This is supported by the large kinetic fragility deduced for all derivatives (Fig. 5). Capturing both diffusion and rotation is hence key in order to accurately describe the relaxation processes in the fragile perylene derivatives studied in this work.

Both the normal vector ACF and the diffusivity systematically overestimate the glass transition temperature and the kinetic fragility compared to experiment. The overestimation of the kinetic fragility suggests that the processes represented by τ_3 in the MD simulation are slower than those encountered during experiments. This could be caused by the intermolecular interactions in the simulation being somewhat too soft, which would point toward a limitation in the accuracy of the underlying force field. Another possible explanation could be that the normal vector ACF overestimates the time scale of processes in the system.

As noted in the introduction, experimentally the glass transition can also be detected as a change in the thermal expansion of the material, an approach that is also occasionally adopted in simulations [22–26]. It is therefore instructive to contrast this approach with the one based on diffusivity and time ACFs used in the present work. For the present systems we observe a change in the thermal expansion coefficient at a temperature of around 400 K, which would suggest much higher glass transition temperatures (Sect. S6). At the same time, one can observe from the analysis of the normal vector ACF that in this temperature range the relaxation time for the slowest process τ_3 reaches the limit of the MD time scale. The change in the thermal expansion is thus merely a direct result of the latter rather than a feature of the system. As a result, at least for the present systems the analysis of the thermal expansion cannot be expected to yield a physically meaningful estimate of the glass transition temperature.

The method for extending the temperature range using Bayesian regression presented in this work allows us to study relaxation processes in liquid and supercooled liquid systems containing hundreds to thousands

of molecules. Hence, it is possible to make material-specific predictions for the glass transition temperature and the kinetic fragility. The general approach is directly extendable to other systems, where especially the diffusivity can be readily computed. This work serves as a first step towards accurately describing the complex relaxation processes in multi-component mixtures of perylene derivatives. Insight into these relaxation processes is key in obtaining a systematic understanding of the dynamics of perylene derivatives, enabling the design of stronger and more stable glass forming system.

COMPUTATIONAL DETAILS

MD simulations were performed using the GROMACS package [27] with the OPLS all-atom force field [28]. Topology and structure files where generated using the LigParGen server [29–31], starting from structures from the automated topology builder and repository [32–34]. A time step of 1 fs was used for all simulations, in combination with constraining the hydrogen atoms using the linear constraint solver algorithm [35]. The simulation cell contained between 500 and 2000 molecules depending on the length of the alkyl chain of the perylene derivative, and simulations were performed at temperatures in the range 400 K to 800 K.

Each system was equilibrated at the target temperature prior to production using the following protocol. First, the system energy was minimized using a steepest descent optimizer, after which a simulation of 1 ns was performed in the NVT ensemble. This was followed by a 1 ns run in the NPT ensemble at a pressure of 2 kbar using a Berendsen barostat [36] to avoid cavitation. The high-pressure NPT simulation was followed by a 10 ns NPT simulation at 1 bar. Finally, production runs were carried out in the NPT ensemble using the stochastic pressure-rescaling barostat and a stochastic velocity-rescaling thermostat [37] to obtain the diffusivity as well as the short and long-time normal vector ACF (Sect. S1). The production runs were 100 ps and 10 ns long, and trajectory files were written every 1 fs and 100 fs, respectively.

The trajectories resulting from the simulations were then parsed using the MDTRAJ package [38] and analyzed using PYTHON scripts to compute the correlation function defined by Eq. 2. Bayesian regression analysis was performed using the NUMPY [39], PANDAS [40, 41], SCIPY [42] and EMCEE [43] packages. Plots were generated using MATPLOTLIB [44], SEABORN [45], CORNER [46], and color maps from PERFECT-CMAPS [47].

ACKNOWLEDGMENTS

We are grateful to Göran Wahnström for helpful discussions. This work was funded by the Swedish Foundation for Strategic Research via the SwedNESS graduate school (GSn15-0008), the Swedish Research Council (grant numbers 2019-04020, 2020-04935, 2021-05072, 2022-02977), and the Chalmers Initiative for Advancement of Neutron and Synchrotron Techniques. The computations were enabled by resources provided by the National Academic Infrastructure for Supercomputing in Sweden (NAISS) at C3SE, NSC, and PDC partially funded by the Swedish Research Council through grant agreements no. 2022-06725 and no. 2018-05973.

[1] G. Zhang, F. R. Lin, F. Qi, T. Heumüller, A. Distler, H.-J. Egelhaaf, N. Li, P. C. Y. Chow, C. J. Brabec, A. K.-Y. Jen, and H.-L. Yip, Renewed Prospects for Organic Photovoltaics, Chemical Reviews **122**, 14180 (2022).

[2] L. Zhu, M. Zhang, Z. Zhou, W. Zhong, T. Hao, S. Xu, R. Zeng, J. Zhuang, X. Xue, H. Jing, Y. Zhang, and F. Liu, Progress of organic photovoltaics towards 20% efficiency, Nature Reviews Electrical Engineering **1**, 581 (2024).

[3] J. Hou, O. Inganäs, R. H. Friend, and F. Gao, Organic solar cells based on non-fullerene acceptors, Nature Materials **17**, 119 (2018).

[4] H. Tang, Z. Liao, Q. Chen, H. Xu, J. Huang, J. Han, D. Hu, Y. Luo, S. Lu, D. Baran, G. Li, C. J. Brabec, F. Laquai, and Y. He, Elucidating the optimal material combinations of organic photovoltaics for maximum industrial viability, Joule **8**, 2208 (2024).

[5] C. R. Snyder and D. M. DeLongchamp, Glassy phases in organic semiconductors, Current Opinion in Solid State and Materials Science Materials Design of Glasses, **22**, 41 (2018).

[6] J. M. Ha, S. H. Hur, A. Pathak, J.-E. Jeong, and H. Y. Woo, Recent advances in organic luminescent materials with narrowband emission, NPG Asia Materials **13**, 1 (2021).

[7] T. Chiba, Y.-J. Pu, and J. Kido, White OLED (WOLED) and Charge Generation Layer (CGL), in *Handbook of Organic Light-Emitting Diodes*, edited by C. Adachi, R. Hattori, H. Kaji, and T. Tsujimura (Springer Japan, Tokyo, 2018) pp. 1–22.

[8] R. J. Salthouse and K. Moth-Poulsen, Multichromophoric photoswitches for solar energy storage: From azobenzene to norbornadiene, and MOST things in between, Journal of Materials Chemistry A **12**, 3180 (2024).

[9] Z. Wang, H. Hölzel, and K. Moth-Poulsen, Status and challenges for molecular solar thermal energy storage system based devices, Chemical Society Reviews **51**, 7313 (2022).

[10] M. Uji, T. J. B. Zähringer, C. Kerzig, and N. Yanai, Visible-to-UV Photon Upconversion: Recent Progress in New Materials and Applications, Angewandte Chemie International Edition **62**, e202301506 (2023).

[11] C. Müller, On the Glass Transition of Polymer Semiconductors and Its Impact on Polymer Solar Cell Stability, Chemistry of Materials **27**, 2740 (2015).

[12] S. Hultmark, A. Cravcenco, K. Kushwaha, S. Mallick, P. Erhart, K. Börjesson, and C. Müller, Vitrification of octonary perylene mixtures with ultralow fragility, Science Advances **7**, eabi4659 (2021).

[13] S. H. K. Paleti, S. Hultmark, J. Han, Y. Wen, H. Xu, S. Chen, E. Järsvall, I. Jalan, D. R. Villalva, A. Sharma, J. I. Khan, E. Moons, R. Li, L. Yu, J. Gorenflot, F. Laquai, C. Müller, and D. Baran, Hexanary blends: A strategy towards thermally stable organic photovoltaics, Nature Communications **14**, 4608 (2023).

[14] G. Wahnström, Molecular-dynamics study of a supercooled two-component Lennard-Jones system, Physical Review A **44**, 3752 (1991).

[15] L. J. Lewis and G. Wahnström, Relaxation of a molecular glass at intermediate times, Solid State Communications **86**, 295 (1993).

[16] D. Frenkel and B. Smit, *Understanding Molecular Simulation*, 2nd ed. (Academic Press, Inc., USA, 2001).

[17] J. Rault, Origin of the Vogel–Fulcher–Tammann law in glass-forming materials: The α–β bifurcation, Journal of Non-Crystalline Solids **271**, 177 (2000).

[18] A. Pipertzis, N. Abdou, J. Xu, L. E. Asp, A. Martinelli, and J. Swenson, Ion transport, mechanical properties and relaxation dynamics in structural battery electrolytes consisting of an imidazolium protic ionic liquid confined into a methacrylate polymer, Energy Materials **3**, 300050 (2023).

[19] K. L. Ngai, G. Floudas, D. J. Plazek, and A. K. Rizos, Amorphous Polymers, in *Encyclopedia of Polymer Science and Technology* (John Wiley & Sons, Ltd, 2002).

[20] L. J. Lewis and G. Wahnström, Molecular-dynamics study of supercooled ortho-terphenyl, Physical Review E **50**, 3865 (1994).

[21] A. Saiter, J. M. Saiter, and J. Grenet, Cooperative rearranging regions in polymeric materials: Relationship with the fragility of glass-forming liquids, European Polymer Journal **42**, 213 (2006).

[22] P. N. Patrone, A. Dienstfrey, A. R. Browning, S. Tucker, and S. Christensen, Uncertainty quantification in molecular dynamics studies of the glass transition temperature, Polymer **87**, 246 (2016).

[23] M. Reisjalali, J. Javier Burgos-Mármol, R. Manurung, and A. Troisi, Local structuring of diketopyrrolopyrrole (DPP)-based oligomers from molecular dynamics simulations, Physical Chemistry Chemical Physics **23**, 19693 (2021).

[24] C. P. Callaway, J. H. Bombile, W. Mask, S. M. Ryno, and C. Risko, Thermomechanical enhancement of DPP-4T through purposeful π-conjugation disruption, Journal of Polymer Science **60**, 559 (2022).

[25] N. Farzi and M. Ebrahim, Mechanical properties and glass transition temperature of metal-organic framework-filled epoxy resin: A molecular dynamics study, Materials Chemistry and Physics **314**, 128874 (2024).

[26] N. Marchin, S. Urata, and J. Du, Effect of three-body interaction on structural features of phosphate glasses from molecular dynamics simulations, The Journal of Chemical Physics **161**, 154507 (2024).

[27] M. J. Abraham, T. Murtola, R. Schulz, S. Páll, J. C. Smith, B. Hess, and E. Lindahl, GROMACS: High performance molecular simulations through multi-level parallelism from laptops to supercomputers, SoftwareX **1–2**, 19 (2015).

[28] W. L. Jorgensen and J. Tirado-Rives, The OPLS [optimized potentials for liquid simulations] potential functions for proteins, energy minimizations for crystals of cyclic peptides and crambin, Journal of the American Chemical Society **110**, 1657 (1988).

[29] W. L. Jorgensen and J. Tirado-Rives, Potential energy functions for atomic-level simulations of water and organic and biomolecular systems, Proceedings of the National Academy of Sciences **102**, 6665 (2005).

[30] L. S. Dodda, J. Z. Vilseck, J. Tirado-Rives, and W. L. Jorgensen, 1.14*CM1A-LBCC: Localized Bond-Charge Corrected CM1A Charges for Condensed-Phase Simulations, The Journal of Physical Chemistry B **121**, 3864 (2017).

[31] L. S. Dodda, I. Cabeza de Vaca, J. Tirado-Rives, and W. L. Jorgensen, LigParGen web server: An automatic OPLS-AA parameter generator for organic ligands, Nucleic Acids Research **45**, W331 (2017).

[32] A. K. Malde, L. Zuo, M. Breeze, M. Stroet, D. Poger, P. C. Nair, C. Oostenbrink, and A. E. Mark, An Automated Force Field Topology Builder (ATB) and Repository: Version 1.0, Journal of Chemical Theory and Computation **7**, 4026 (2011).

[33] S. Canzar, M. El-Kebir, R. Pool, K. Elbassioni, A. K. Malde, A. E. Mark, D. P. Geerke, L. Stougie, and G. W. Klau, Charge Group Partitioning in Biomolecular Simulation, Journal of Computational Biology **20**, 188 (2013).

[34] K. B. Koziara, M. Stroet, A. K. Malde, and A. E. Mark, Testing and validation of the Automated Topology Builder (ATB) version 2.0: Prediction of hydration free enthalpies, Journal of Computer-Aided Molecular Design **28**, 221 (2014).

[35] B. Hess, H. Bekker, H. J. C. Berendsen, and J. G. E. M. Fraaije, LINCS: A linear constraint solver for molecular simulations, Journal of Computational Chemistry **18**, 1463 (1997).

[36] H. J. C. Berendsen, J. P. M. Postma, W. F. van Gunsteren, A. DiNola, and J. R. Haak, Molecular dynamics with coupling to an external bath, The Journal of Chemical Physics **81**, 3684 (1984).

[37] G. Bussi, D. Donadio, and M. Parrinello, Canonical sampling through velocity rescaling, The Journal of Chemical Physics **126**, 014101 (2007).

[38] R. T. McGibbon, K. A. Beauchamp, M. P. Harrigan, C. Klein, J. M. Swails, C. X. Hernández, C. R. Schwantes, L.-P. Wang, T. J. Lane, and V. S. Pande, MDTraj: A Modern Open Library for the Analysis of Molecular Dynamics Trajectories, Biophysical Journal **109**, 1528 (2015).

[39] C. R. Harris, K. J. Millman, S. J. van der Walt, R. Gommers, P. Virtanen, D. Cournapeau, E. Wieser, J. Taylor, S. Berg, N. J. Smith, R. Kern, M. Picus, S. Hoyer, M. H. van Kerkwijk, M. Brett, A. Haldane, J. F. del Río, M. Wiebe, P. Peterson, P. Gérard-Marchant, K. Sheppard, T. Reddy, W. Weckesser, H. Abbasi, C. Gohlke, and T. E. Oliphant, Array programming with NumPy, Nature **585**, 357 (2020).

[40] W. McKinney, Data Structures for Statistical Computing in Python, scipy 10.25080/Majora-92bf1922-00a (2010).

[41] The pandas development team, Pandas-dev/pandas: Pandas (2023).

[42] P. Virtanen, R. Gommers, T. E. Oliphant, M. Haberland, T. Reddy, D. Cournapeau, E. Burovski, P. Peterson, W. Weckesser, J. Bright, S. J. van der Walt, M. Brett, J. Wilson, K. J. Millman, N. Mayorov, A. R. J. Nelson, E. Jones, R. Kern, E. Larson, C. J. Carey, İ. Polat, Y. Feng, E. W. Moore, J. VanderPlas, D. Laxalde, J. Perktold, R. Cimrman, I. Henriksen, E. A. Quintero, C. R. Harris, A. M. Archibald, A. H. Ribeiro, F. Pedregosa, and P. van Mulbregt, SciPy 1.0: Fundamental algorithms for scientific computing in Python, Nature Methods **17**, 261 (2020).

[43] D. Foreman-Mackey, D. W. Hogg, D. Lang, and J. Goodman, Emcee: The MCMC Hammer (2013), arXiv:1202.3665.

[44] J. D. Hunter, Matplotlib: A 2D Graphics Environment, Computing in Science & Engineering **9**, 90 (2007).

[45] M. L. Waskom, Seaborn: Statistical data visualization, Journal of Open Source Software **6**, 3021 (2021).

[46] D. Foreman-Mackey, Corner.py: Scatterplot matrices in Python, Journal of Open Source Software **1**, 24 (2016).

[47] M. Ulmestrand, Perfect-cmaps (2024).

Supporting Information

Probing Glass Formation in Perylene Derivatives via Atomic Scale Simulations and Bayesian Regression

Eric Lindgren[1], Jan Swensson[1], Christian Müller[2], and Paul Erhart[1,*]

[1] *Department of Physics, Chalmers University of Technology, SE-412 96 Gothenburg, Sweden*
[1] *Department of Chemistry and Chemical Technology, Chalmers University of Technology, SE-412 96 Gothenburg, Sweden*
[*] *erhart@chalmers.se*

Contents

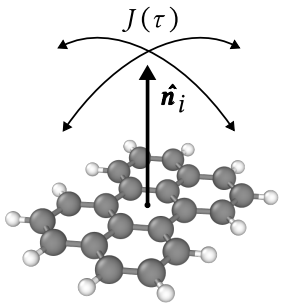

Figure S1: Schematic representation of the normal vector autocorrelation function $J(\tau)$, see Eq. (S3).

S1 Computing the normal vector autocorrelation function

Given $\boldsymbol{r}_i^m(t)$ as the position of atom m in molecule i at time t, the centroid position of molecule i with M atoms is defined as

$$\boldsymbol{r}_i(t) = \frac{1}{M}\sum_{m=1}^{M} \boldsymbol{r}_i^m(t). \tag{S1}$$

We can now define the normal vector correlation function,

$$C_{\hat{n}\hat{n}}(r,\tau) = \left\langle \sum_{i=1}^{N}\sum_{j=1}^{N} \delta(\boldsymbol{r}-\boldsymbol{r}_{ij})\hat{\boldsymbol{n}}_i(t)\cdot\hat{\boldsymbol{n}}_j(t+\tau)\right\rangle_t, \tag{S2}$$

where $\hat{\boldsymbol{n}}_i(t)$ is the normal vector of molecule i, and is calculated by computing the normal to the point cloud of atoms in the molecule, $\{\boldsymbol{r}_i^m(t)\}$. The ensemble average is taken over all frames in the trajectory. In particular, we study the special case of the normal vector autocorrelation function $C_{\hat{n}\hat{n}}(0,\tau)$, denoted $J(\tau)$.

$$J(\tau) = C_{\hat{n}\hat{n}}(\tau) = \langle \hat{\boldsymbol{n}}_i(t)\cdot\hat{\boldsymbol{n}}_i(t+\tau)\rangle_{it}, \tag{S3}$$

with the ensemble average taken over all frames t and each molecule i in the system. Equation (S3) can be efficiently computed from the signal $\hat{\boldsymbol{n}}_i(t)$ using the Wiener-Kinchin theorem.

We may also extract the standard error as an uncertainty estimate for $J(\tau)$ from the correlation function for each molecule $J_i(\tau)$ before computing the ensemble average in equation Eq. S3, using the central limit theorem,

$$\sigma_J(\tau) = \sqrt{\mathrm{Var}\left(\{J_i\}_{i=1}^N\right)}/\sqrt{N}, \tag{S4}$$

where N is the number of molecules in the system. The normal vector $\hat{n}_i(t)$ and $J(\tau)$ are schematically represented in Fig. S1.

Two production molecular dynamics (MD) simulations, with a length of 100 ps and 10 ns respectively, were run in order to get the same number of statistics for short and long timelags. The trajectory files were written every 1 fs for the 100 ps simulation and every 100 fs for the 10 ns simulation. The normal vector autocorrelation functions (ACFs) according to Eq. S3 were calculated for both production runs and then spliced together at a time lag of $\tau = 1$ ps. This splicing was also done for the standard error in equation Eq. S4.

S2 Extracting the diffusivity from the mean-squared displacement

We obtained the molecular diffusivity D for each perylene derivative **I**–**V** and temperature, from the mean squared displacement (MSD) $\langle \Delta r^2 \rangle$ of the molecular centroid positions[1],

$$\langle \Delta r^2 \rangle = 6D\tau. \tag{S5}$$

The diffusivity was computed using production runs with a duration of up to 10 ns. D was extracted by performing a linear fit using Bayesian regression to the MSD (Fig. S2). Note that D for

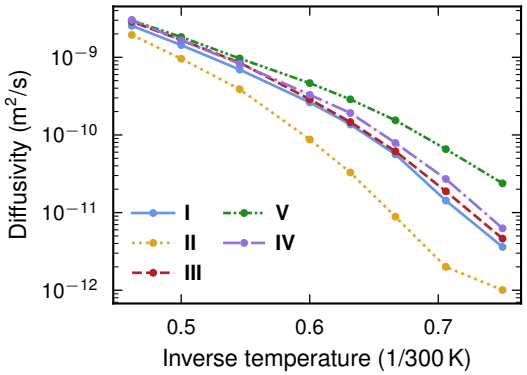

Figure S2: Diffusivity computed from the MSD for each perylene derivative **I**–**V**

high temperatures change slope; this is due to some of the derivatives transitioning to a gaseous phase. When fitting the Vogel-Fulcher-Tammann (VFT) equation we thus only considered D for temperatures $< 700\,\mathrm{K}$.

S3 Bayesian fitting

In this work, we use a Gaussian likelihood function, which under the assumption of independent and identically distributed N_d data $d_i \in \mathcal{D}$, here takes the form,

$$p(\mathcal{D}|\boldsymbol{\theta}, \mathcal{I}) = \prod_{i=1}^{N_d} \frac{1}{\sqrt{2\pi\sigma_i^2}} e^{-(M(\boldsymbol{\theta})-d_i)^2/(2\sigma_i^2)}, \tag{S6}$$

with σ_i^2 as the variance of the residual for datum d_i. We use σ_i to encode the standard error of the diffusivity and the ACF, as well as to perform error propagation.

S3.1 Fitting the autocorrelation function to triple exponential

Let $J(\tau)_T$ denote the ACF for temperature T. For each perylene derivative a–e, we have a data set of ACFs $\mathcal{D} = \{J(\tau)_{T_i}\}_{i=1}^{L}$, where L is the number of distinct temperatures studied for this derivative. In this stage, we used a Gaussian likelihood on the form in equation Eq. S6, where we let $\sigma_i = \sigma/\sigma_{J(\tau)_{T_i}}$, with $\sigma_{J(\tau)_{T_i}}$ being the standard error for ACF $J(\tau)_{T_i}$ at temperature T_i, and σ is a free parameter. This is a heteroscedastic error model, in which each datum has an individual error. In total, the set of free parameters to optimise in this stage was $\boldsymbol{\theta} = \{A_1, A_2, \tau_1, \tau_2, \tau_3, \beta, \sigma\}$.

The priors for each of the parameters were set as follows,

$$p(A_i|\mathcal{I}) = \frac{1}{0.2} e^{-|A_i/0.1|}, \text{ for } A_1, A_2 \tag{S7}$$

$$p(\tau_1|\mathcal{I}) = \frac{\sqrt{2}}{5\sqrt{\pi}} e^{-(\tau_1/5)^2/2}, x > 0 \tag{S8}$$

$$p(\tau_2|\mathcal{I}) = \frac{1}{50\sqrt{2\pi}} e^{-((\tau_2-10)/50)^2/2} \tag{S9}$$

$$p(\tau_3|\mathcal{I}) = \frac{1}{\sqrt{2\pi}} e^{-(\log_{10}(\tau_3)-3)^2/2} \tag{S10}$$

$$p(\beta|\mathcal{I}) = \frac{\sqrt{2}}{0.1\sqrt{\pi}} e^{-((x-1)/0.1)^2/2}, x = 2-\beta \tag{S11}$$

$$p(\sigma|\mathcal{I}) = \frac{\sqrt{2}}{\sqrt{\pi}} e^{-\sigma^2/2}, x > 0 \tag{S12}$$

with the same priors being used for all temperatures. Note that the prior for τ_3 is for $\log_{10}(\tau_3)$, due to τ_3 spanning several orders of magnitude throughout the temperature range. The joint prior

then becomes

$$\begin{aligned} p(\boldsymbol{\theta}|\mathcal{I}) =& p(A_1|\mathcal{I})p(A_2|\mathcal{I}) \\ & p(\tau_1|\mathcal{I})p(\tau_2|\mathcal{I})p(\tau_3|\mathcal{I}) \\ & p(\beta|\mathcal{I})p(\sigma|\mathcal{I}). \end{aligned} \tag{S13}$$

We then used Markov-chain Monte Carlo (MCMC) sampling to sample the posterior $p(\boldsymbol{\theta}|\mathcal{D},\mathcal{I})$. For numerical stability, the likelihood and priors were rewritten as the log-likelihood and log-prior respectively. Optimizing the posterior or the log-posterior does not change the resulting distributions, and thus the quantity that was optimized was, up to a constant,

$$\ln\left(p(\boldsymbol{\theta}|\mathcal{D},\mathcal{I},T)\right) = \ln\left(p(\mathcal{D}|\boldsymbol{\theta},\mathcal{I},T)\right) + \ln\left(p(\boldsymbol{\theta}|\mathcal{I})\right). \tag{S14}$$

See Sect. S7 and Sect. S8 in the Supplementary Information for traces and corner plots resulting from the Bayesian fitting procedure.

$$J(\tau) = A_1 e^{-\tau/\tau_1} + A_2 e^{-\tau/\tau_2} + (1 - A_1 - A_2)e^{(-\tau/\tau_3)^\beta}, \tag{S15}$$

The triple-exponential model in equation Eq. S15 has six free parameters, and combined with the noise parameter σ we thus obtain a seven-dimensional posterior distribution $p(\boldsymbol{\theta}|\mathcal{D},\mathcal{I},T)$. From the posterior distribution, the marginal distribution for τ_3 can then be extracted,

$$p(\tau_3|\mathcal{D},\mathcal{I},T) \propto \int p(\boldsymbol{\theta}|\mathcal{D},\mathcal{I},T) dA_1 dA_2 d\tau_1 d\tau_2 d\beta d\sigma. \tag{S16}$$

Computationally, the marginal distribution can be extracted by only studying the samples distributions for the marginal parameters of interest. Mean $\mu_{\tau_3}(T)$ and standard deviation $\sigma_{\tau_3}(T)$ of $\tau_3(T)$ were then extracted from $p(\tau_3|\mathcal{D},\mathcal{I},T)$ in order to inform the second stage of the regression process.

S3.2 Fitting the diffusivity and autocorrelation to the VFT equation

Both the diffusivity and τ_3 were fit to a VFT equation using the same framework, as described in this section. The only difference between the two is the sign in the exponential of the VFT equation, which was negative for the diffusivity since the diffusivity decreases with temperature. We present the fitting for τ_3 here as an example.

We fitted a VFT equation the mean values $\tau_3(T)$, $\mu_{\tau_3}(T)$, from the first stage of the process,

$$K(T;\boldsymbol{\theta'}) = \tau_3^0 \exp \frac{B}{k_B(T - T_{\mathrm{VF}})}, \tag{S17}$$

where k_B is the Boltzmann constant. The VFT equation is an experimentally observed law that the non-Arrhenius behaviour of α-relaxation in glass forming systems obeys, where τ_3^0, B, and T_{VF} are empirical fitting parameters[2].

Note that the VFT equation as written in the main paper does not include k_B, and is instead written on the common form $K(T;\boldsymbol{\theta'}) = \tau_3^0 \exp \frac{B}{(T - T_{\mathrm{VF}})}$ However, when actually fitting the VFT equation we introduced k_B for numerical reasons as this yields a value of $B \leq 1$. k_B was then absorbed back into B for all subsequent calculations of T_g, m etc.

The data set consisted of $\mathcal{D}' = \{\mu_{\tau_3}(T_i)\}_{i=1}^L$. In this case also a Gaussian likelihood with heteroscedastic errors $\sigma_i = \sigma'/\sigma_{\tau_3}(T)$ was used, with $\sigma_{\tau_3}(T)$ as the estimated standard deviation of the posterior distribution for τ_3. In total, four free parameters were fitted at this stage, $\boldsymbol{\theta'} = \{\tau_3^0, B, T_{VF}, \sigma'\}$.

The priors used in the second stage of the fitting procedure were,

$$p(\tau_3^0|\mathcal{I}) = \frac{\sqrt{2}}{\sqrt{\pi}} e^{-(\tau_3^0)^2/2}, x > 0 \tag{S18}$$

$$p(B|\mathcal{I}) = \frac{\sqrt{2}}{\sqrt{\pi}} e^{-B^2/2}, x > 0 \tag{S19}$$

$$p(T_{VF}|\mathcal{I}) = \frac{1}{200\sqrt{2}\pi} e^{-(T_{VF}-200)/200)^2/2} \tag{S20}$$

$$p(\sigma'|\mathcal{I}) = \frac{\sqrt{2}}{\sqrt{\pi}} e^{-\sigma'^2/2}, x > 0 \tag{S21}$$

The log-posterior was then optimized using MCMC-sampling, similarly to the first stage of the regression process. See Sect. S7 and Sect. S8 in the Supplementary Information for all traces and corner plots resulting from the Bayesian fitting procedure.

The resulting posterior distribution $p(\boldsymbol{\theta}'|\mathcal{D}', \mathcal{I}')$ of the fit to the VFT equation was then used to extrapolate τ_3 to lower temperatures, feeding the posterior distribution samples through the model in equation Eq. S17. The glass transition temperature T_g is roughly taken to be the temperature at which the slowest relaxation process in the system exceeds $100\,\mathrm{s}$[2]. We therefore took the temperature at which $\tau_3(T)$ exceeded $100\,\mathrm{s}$ for each sample of the posterior distribution as an individual estimate of T_g. In total, for each molecule a–e, we obtained a distribution $p(T_g|\mathcal{D}, \mathcal{D}', \mathcal{I})$ of estimates of the glass transition temperature T_g. Note that the estimate for T_g is relatively stable with regard to the choice of cutoff time for $\tau_3(T)$. Decreasing the time to $1\,\mathrm{s}$ or increasing it to $10\,000\,\mathrm{s}$ changes T_g by $7\,\mathrm{K}$ and $-5\,\mathrm{K}$, respectively. These changes are smaller than the standard deviation of $p(T_g|\mathcal{D}, \mathcal{D}', \mathcal{I})$, which typically is approximately $10\,\mathrm{K}$ to $20\,\mathrm{K}$ for the systems under study.

The glass transition temperature was similarly estimated from the diffusivity $D(T)$ as obtained from the MSD, using the same workflow. In this case, the inverse of the diffusivity was fitted against a VFT equation. The MSD over $100\,\mathrm{s}$ was then calculated as a function of temperature, and T_g was estimated as the temperature at which the MSD reaches $100\,\mathrm{Å}^2$.

S4 Autocorrelation functions for all perylene derivatives

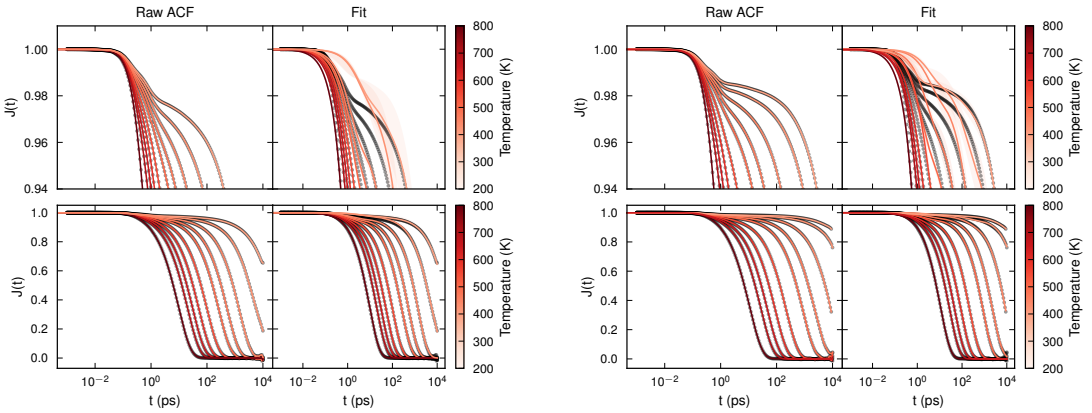

(a) Normal vector ACF for derivative **I**

(b) Normal vector ACF for derivative **II**

Figure S3: Calculated and fitted ACFs using (S15). Error bands of the fits are plus and minus one standard deviation.

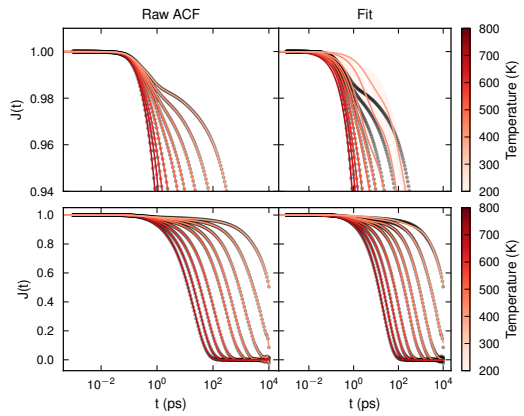

(a) Normal vector ACF for derivative **III**

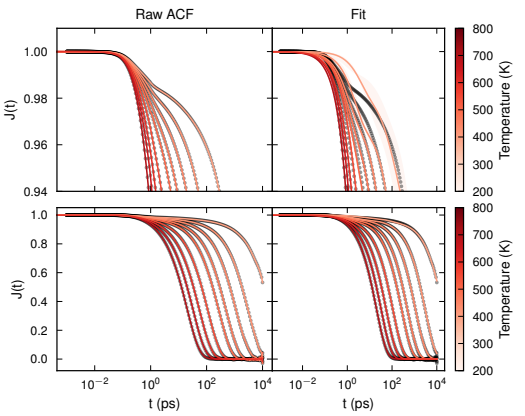

(b) Normal vector ACF for derivative **IV**

Figure S4: Calculated and fitted ACFs using (S15). Error bands of the fits are plus and minus one standard deviation.

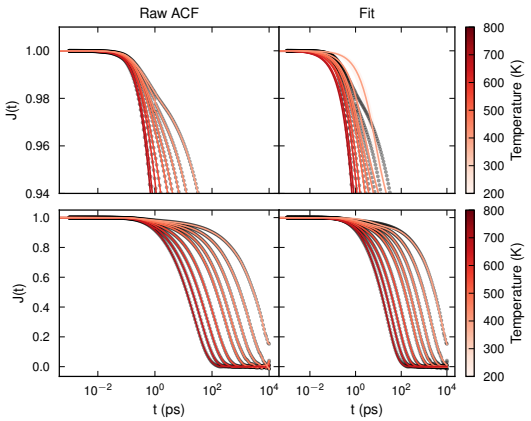

Figure S5: Calculated and fitted ACFs using (S15). Normal vector ACF for derivative **IV**

S5 Decomposing the autocorrelation function

Let $\{\boldsymbol{r}_i^k(t)\}_{k=1}^M$ be a trajectory of the coordinates of the atoms in a specific molecule i. The trajectory of a single molecule i was extracted and the centroid of the molecule, $\boldsymbol{r}_i(t)$, was placed in the middle of the simulation cell for each frame to avoid effects of the molecule moving over the periodic boundaries. The power spectrum of for each Cartesian component of the shifted trajectory was then computed, convoluted with a filter $F(\omega)$ in the Fourier domain, and the filtered power spectrum $S'(\omega)$ was then back transformed to yield a filtered trajectory $\{\boldsymbol{r}_i^{'k}(t)\}_{k=1}^M$,

$$\begin{aligned} S_l(\omega) &= \mathcal{F}\left[r_{il}^k(t)\right]^2(\omega), l \in \{x,y,z\} \\ S_l'(\omega) &= S_l(\omega) * F(\omega) \\ \rightarrow r_{il}^{'k}(t) &= \mathcal{F}^{-1}\left[S_l'(\omega)\right](t) \end{aligned} \tag{S22}$$

where $\mathcal{F}$ denotes the Fourier transform. The filter $F(\omega)$ is a simplified bandpass filter, on the form

$$F(\omega)\begin{cases} 1, & \omega_1 \leq \omega \leq \omega_2 \\ 0, & \text{otherwise.} \end{cases} \tag{S23}$$

By setting the filter frequencies ω_1 and ω_2 to match the expected time scales for τ_1, τ_2 and τ_3, this scheme gives a rough decomposition into what types of motion take place on the different timescales and allows us to somewhat elucidate what processes the ACF capture.

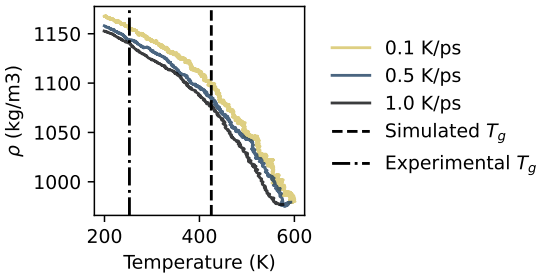

Figure S6: Glass transition temperature T_g estimated via simulated annealing using three different cooling rates for ethyl-perylene, a perylene derivative denoted II in this work. T_g is taken as the point at which the slope of the density changes, roughly at 425 K. This estimate from simulated annealing is severely overestimated compared to the experimentally measured glass transition temperature of 252.35 K from [3].

S6 Estimating the glass transition temperature from simulated annealing

Here we demonstrate the use of simulated annealing for predicting the glass transition temperature of derivative **II** Fig. S6. Following the general approach set out in the literature, T_g is taken as the point at which the density changes slope[4–6]. This approach yields T_g that is overstimated by approximately 150 K, compared to experiments using differential scanning calorimetry from [3].

S7 MCMC sampling

Note that all the traces presented in this section have been sub-sampled by the maximum autocorrelation time over all chains. The traces thus only contain uncorrelated values.

S7.1 MCMC traces: Fitting the diffusivity

In the interest of space, we only show a representative trace plot for derivative **I** at 450 K (Fig. S7). All traces for the remianing perylene derivatives and temperatures are similar.

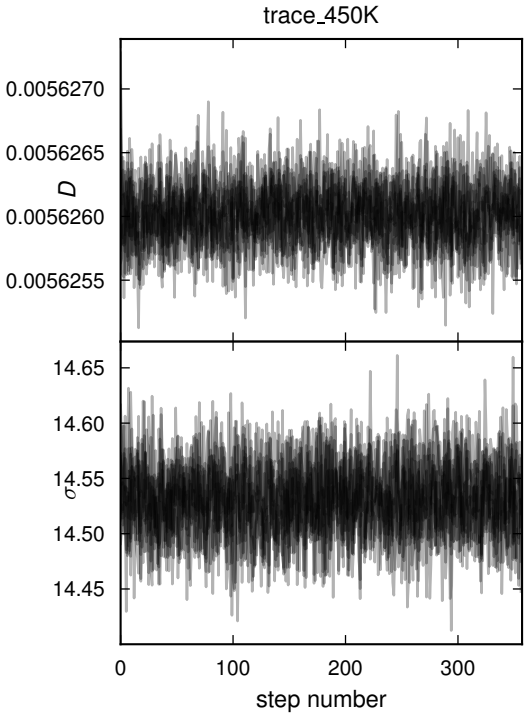

Figure S7: MCMC parameter trace for fitting the diffusivity in equation (S5) to the MSD at 450 K for derivative **I**

S7.2 MCMC traces: Fitting the VFT equation to the diffusivity

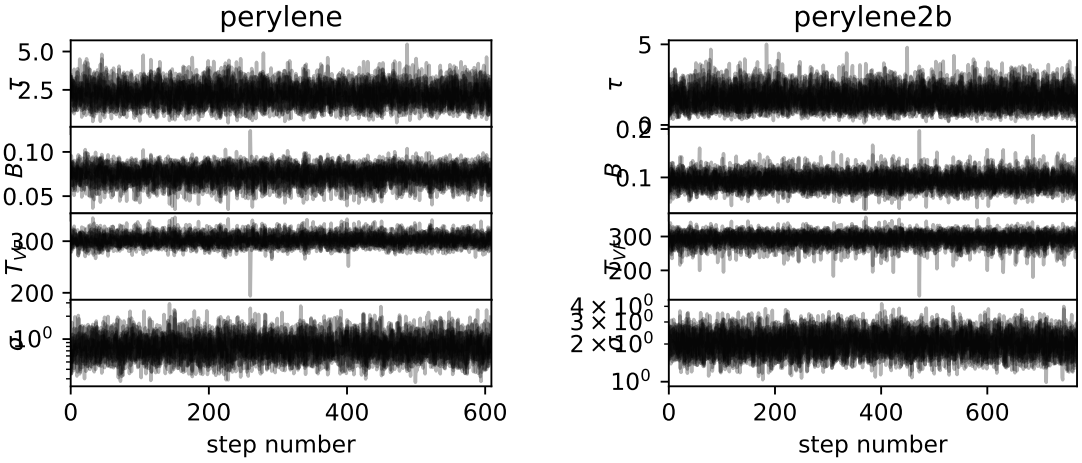

(a) Derivative **I**

(b) Derivative **II**

Figure S8: MCMC parameter trace for the fit of the VFT equation to the diffusivity.

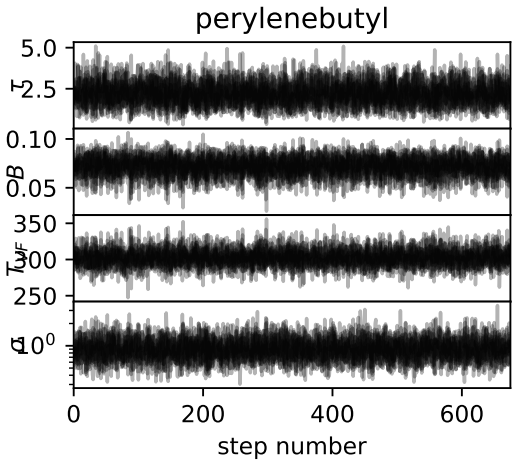

(a) Derivative **III**

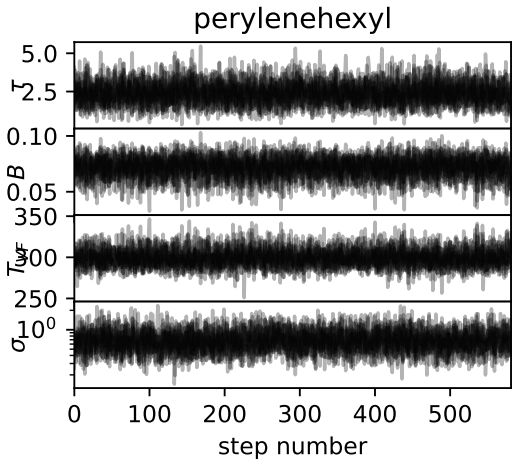

(b) Derivative **IV**

Figure S9: MCMC parameter trace for the fit of the VFT equation to the diffusivity.

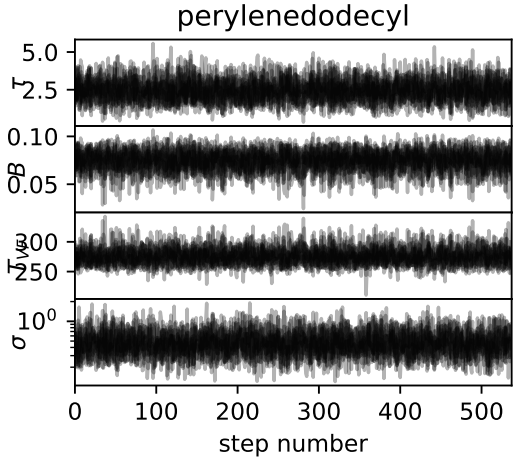

Figure S10: MCMC parameter trace for the fit of the VFT equation to the diffusivity for derivative **V**

S7.3 MCMC traces: Fitting the normal vector ACF

In the interest of space, we only show a representative trace plot for derivative **I** at 450 K (Fig. S11). All traces for the remianing perylene derivatives and temperatures are similar.

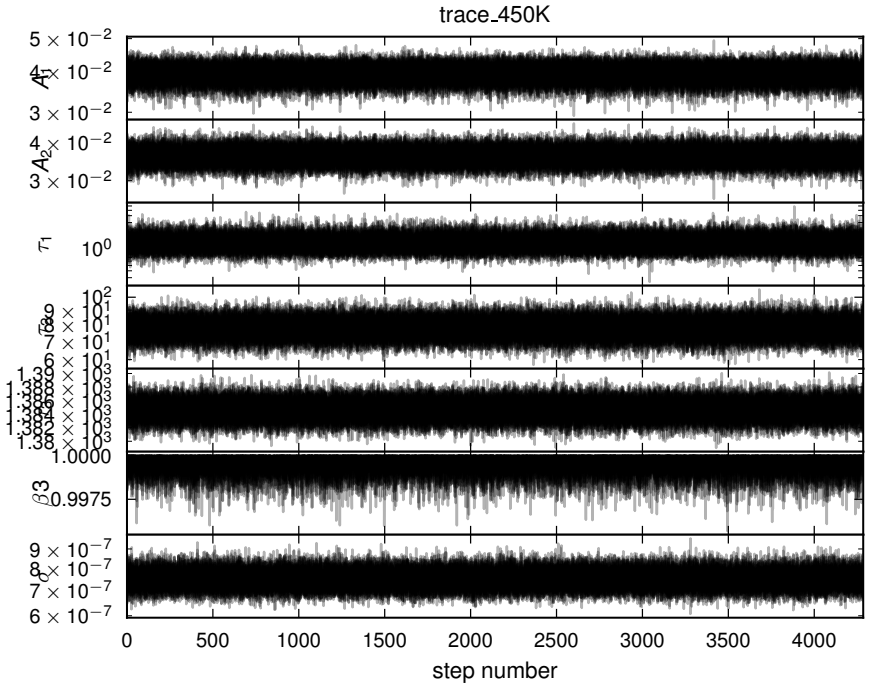

Figure S11: MCMC parameter trace for fitting the triple exponential function in equation (S15) to the normal vector ACF at 450 K for derivative **I**

S7.4 MCMC traces: Fitting the VFT equation to the normal vector ACF

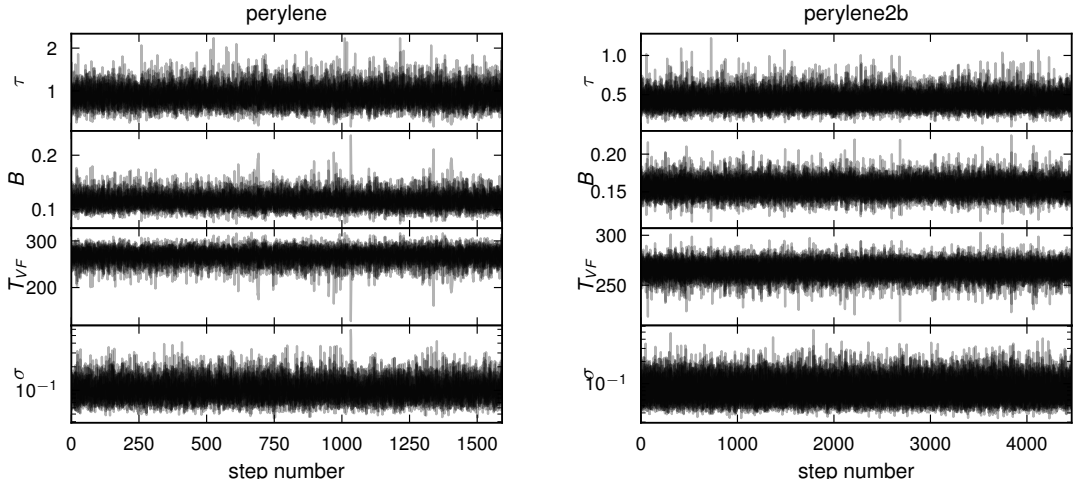

(a) Derivative **I**

(b) Derivative **II**

Figure S12: MCMC parameter trace for the fit of the VFT equation to the normal vector ACF.

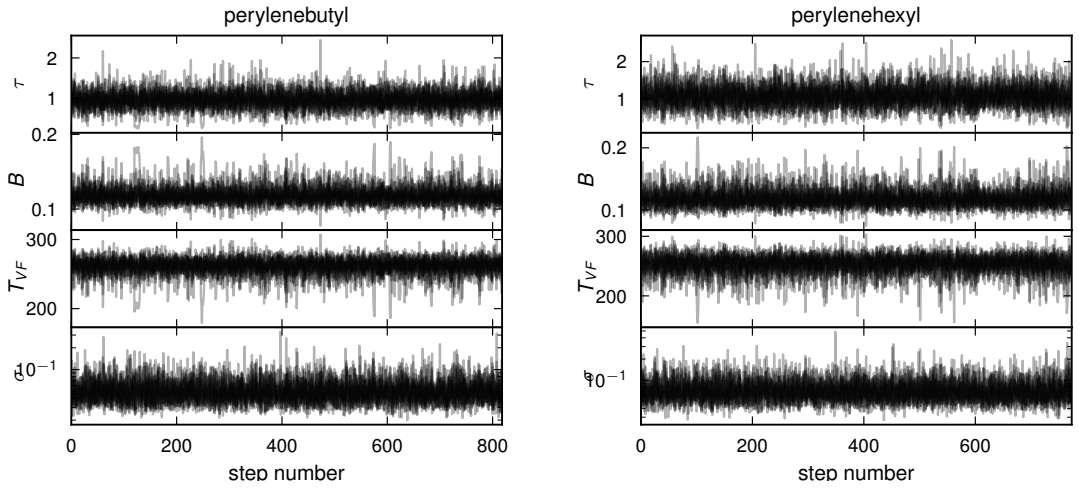

(a) Derivative **III** (b) Derivative **IV**

Figure S13: MCMC parameter trace for the fit of the VFT equation to the normal vector ACF.

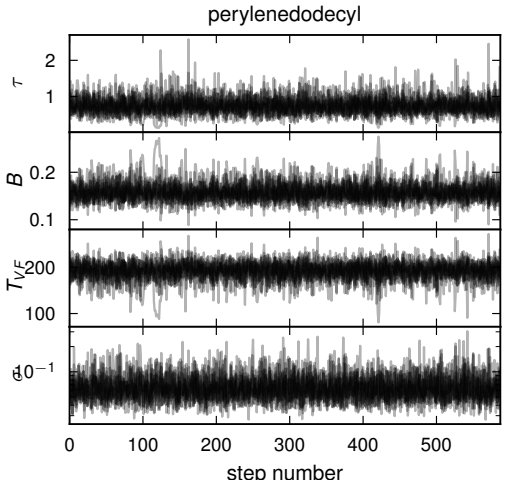

Figure S14: MCMC parameter trace for the fit of the VFT equation to the normal vector ACF for derivative **V**.

S8 Corner plots

Note that all the traces presented in this section have been sub-sampled by the maximum autocorrelation time over all chains. Thus, the corner plots only contain uncorrelated values.

S8.1 Corner plots: Fitting the diffusivity

In the interest of space, we only show a representative corner plot for derivative **I** at 450 K (Fig. S15). All corner plots for the remianing perylene derivatives and temperatures are similar.

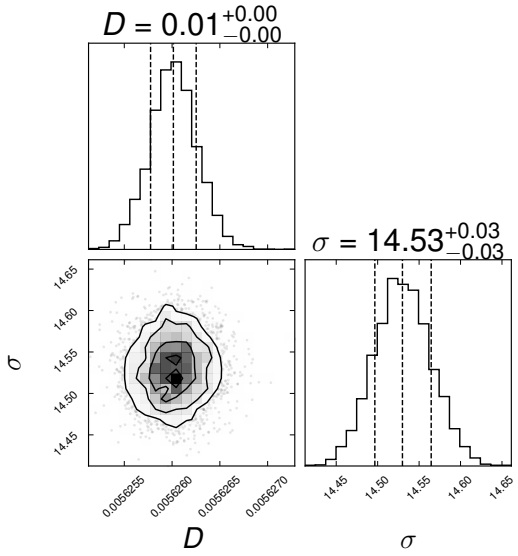

Figure S15: Corner plot of the MCMC parameter samples for fitting the diffusivity in equation (S5) to the MSD at 450 K for derivative **I**.

S8.2 Corner plots: Fitting the VFT equation to the diffusivity

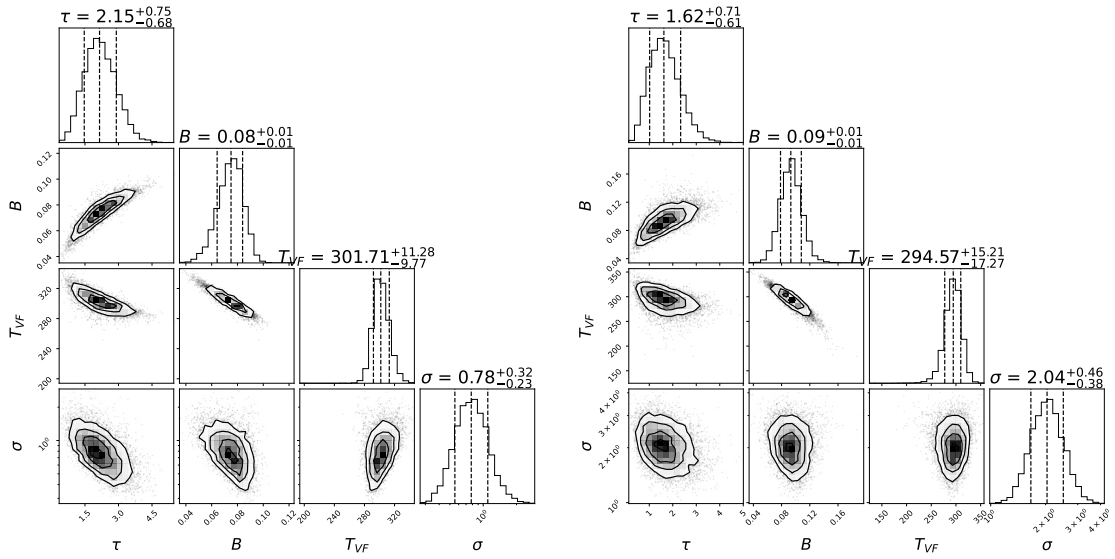

(a) Derivative **I** (b) Derivative **II**

Figure S16: Corner plot for the fit of the VFT equation to the diffusivity.

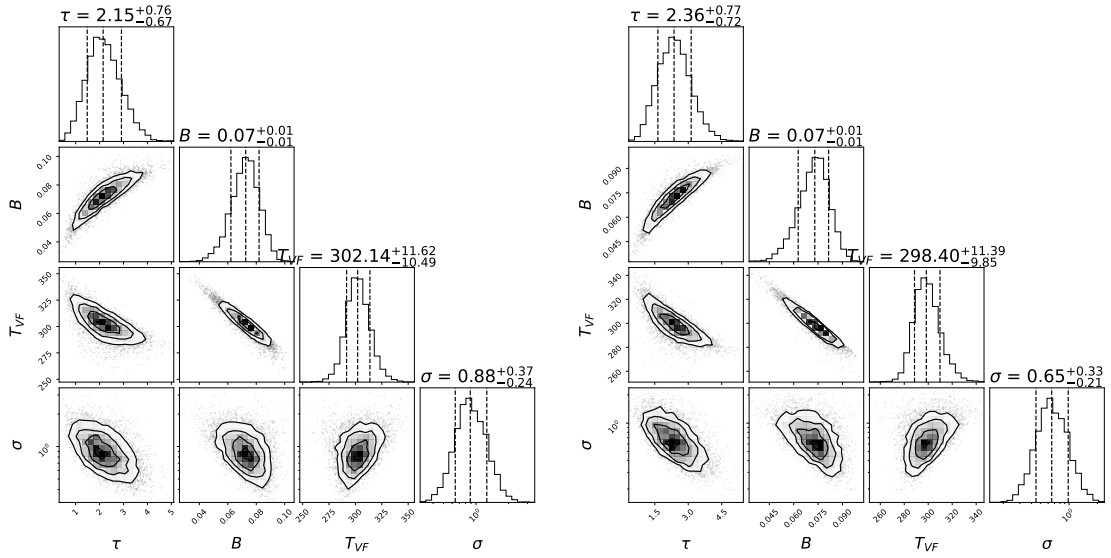

(a) Derivative **III** (b) Derivative **IV**

Figure S17: Corner plot for the fit of the VFT equation to the diffusivity.

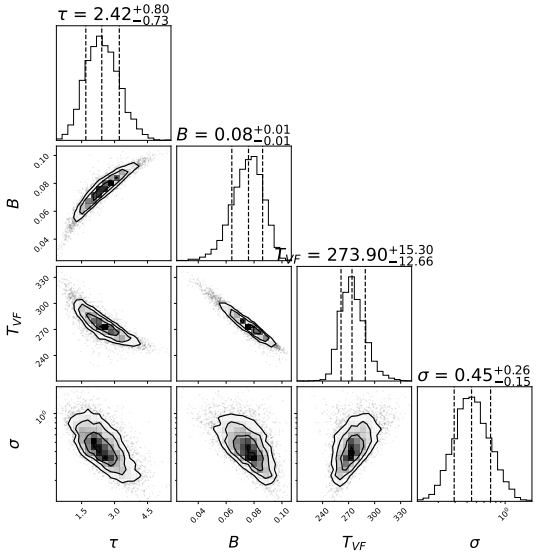

Figure S18: Corner plot for the fit of the VFT equation to the diffusivity for derivative **V**

S8.3 Corner plots: Fitting the normal vector ACF

In the interest of space, we only show a representative corner plot for derivative **I** at 450 K (Fig. S19). All corner plots for the remianing perylene derivatives and temperatures are similar.

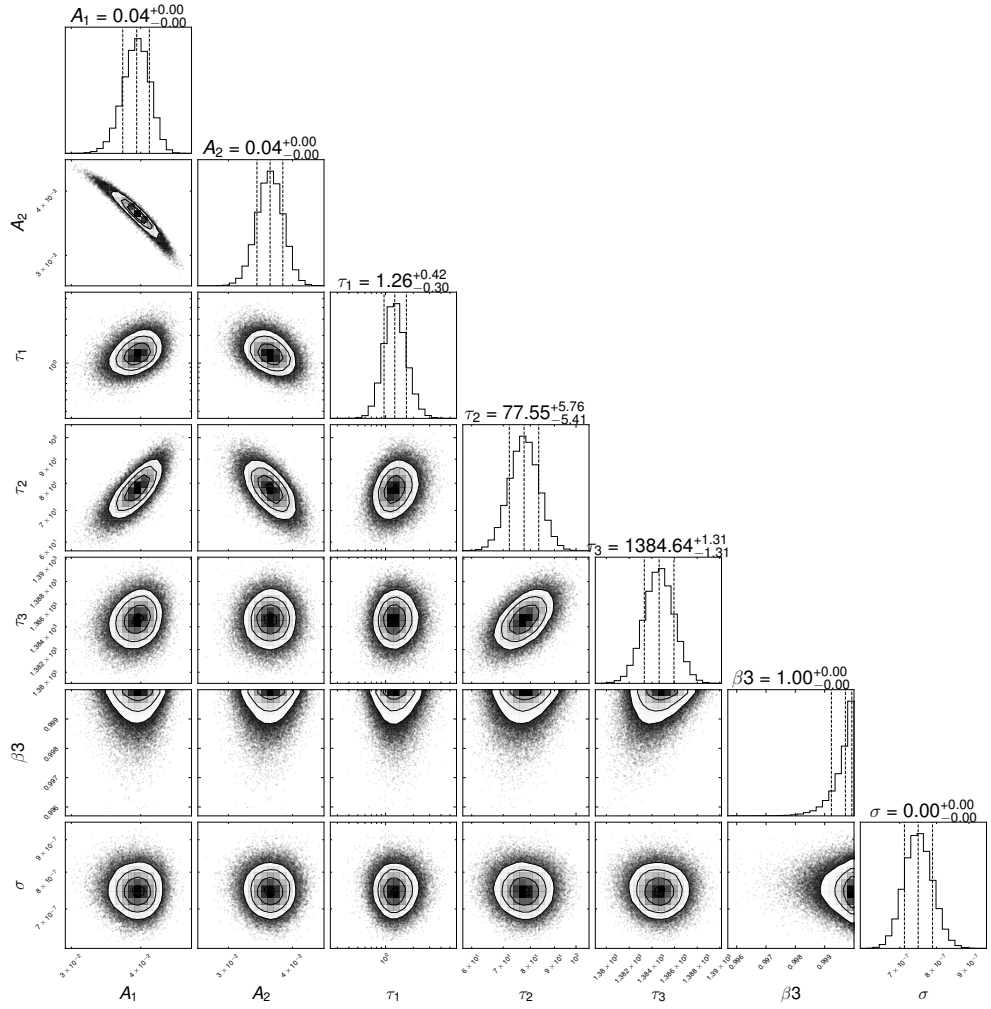

Figure S19: Corner plot of the MCMC parameter samples for fitting the triple exponential function in (S15) to the normal vector ACF at 450 K for derivative **I**.

S8.4 Corner plots: Fitting the VFT equation to the normal vector ACF

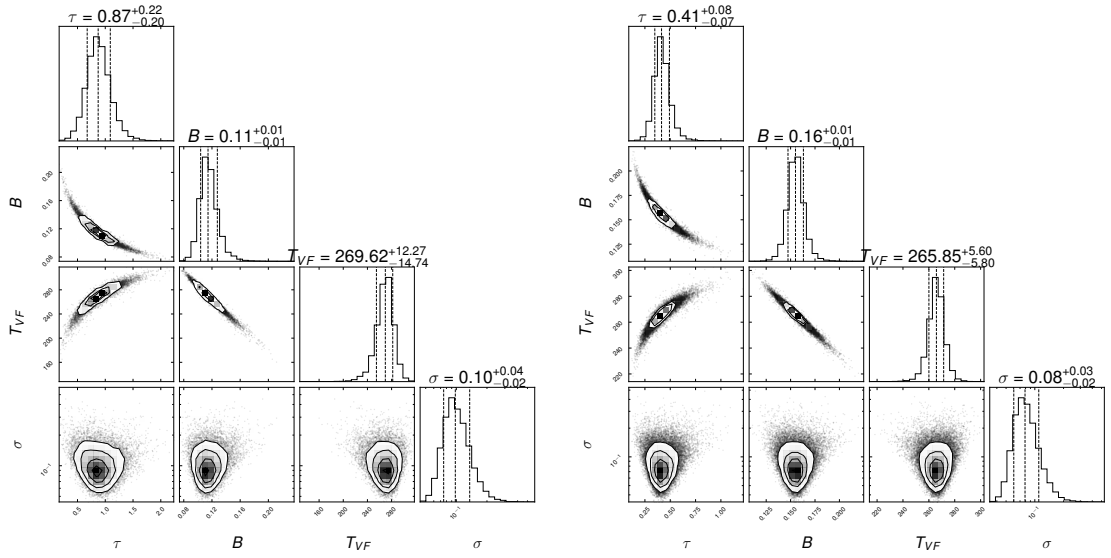

(a) Derivative **I** (b) Derivative **II**

Figure S20: Corner plot for the fit of the VFT equation to the normal vector ACF.

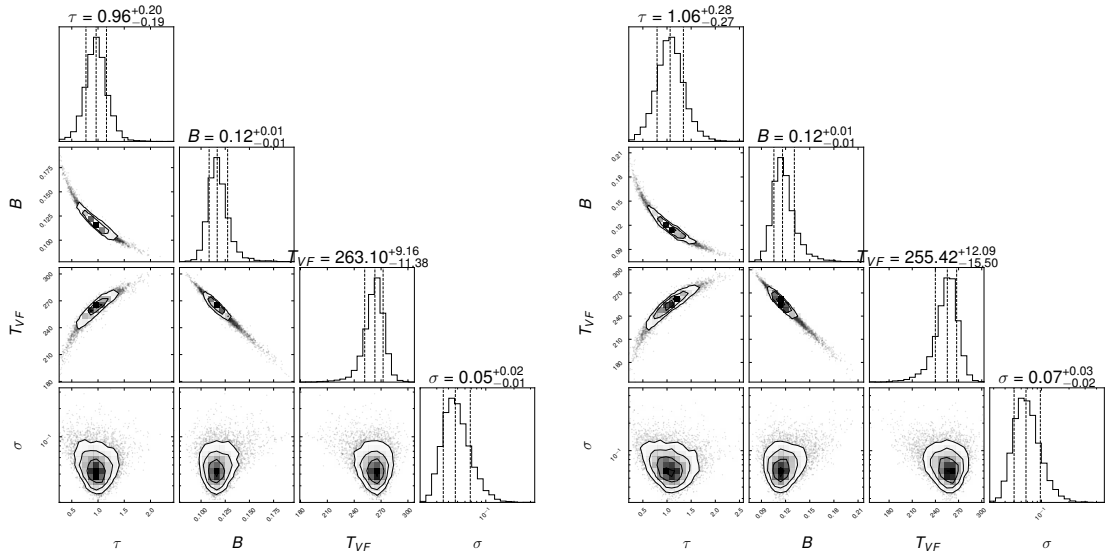

(a) Derivative **III** (b) Derivative **IV**

Figure S21: Corner plot for the fit of the VFT equation to the normal vector ACF.

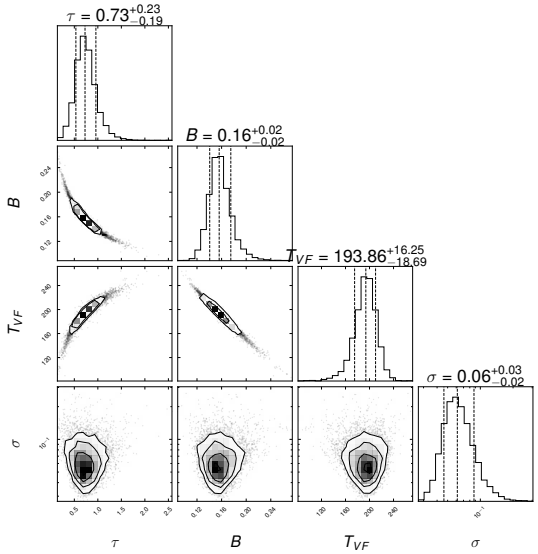

Figure S22: Corner plot for the fit of the VFT equation to the normal vector ACF for derivative **V**.

References

[1] Daan Frenkel and Berend Smit. *Understanding Molecular Simulation*. Academic Press, Inc., USA, 2nd edition, September 2001. ISBN 978-0-12-267351-1.

[2] Jacques Rault. Origin of the Vogel–Fulcher–Tammann law in glass-forming materials: The α–β bifurcation. *Journal of Non-Crystalline Solids*, 271(3):177–217, July 2000. ISSN 0022-3093. doi: 10.1016/S0022-3093(00)00099-5. URL https://www.sciencedirect.com/science/article/pii/S0022309300000995.

[3] Sandra Hultmark, Alex Cravcenco, Khushbu Kushwaha, Suman Mallick, Paul Erhart, Karl Börjesson, and Christian Müller. Vitrification of octonary perylene mixtures with ultralow fragility. *Science Advances*, 7(29):eabi4659, July 2021. ISSN 2375-2548. doi: 10.1126/sciadv.abi4659. URL https://advances.sciencemag.org/lookup/doi/10.1126/sciadv.abi4659.

[4] Nahid Farzi and Maede Ebrahim. Mechanical properties and glass transition temperature of metal-organic framework-filled epoxy resin: A molecular dynamics study. *Materials Chemistry and Physics*, 314:128874, February 2024. ISSN 0254-0584. doi: 10.1016/j.matchemphys.2023.128874. URL https://www.sciencedirect.com/science/article/pii/S0254058423015821.

[5] Navid Marchin, Shingo Urata, and Jincheng Du. Effect of three-body interaction on structural features of phosphate glasses from molecular dynamics simulations. *The Journal of Chemical Physics*, 161(15):154507, October 2024. ISSN 0021-9606. doi: 10.1063/5.0225188. URL https://doi.org/10.1063/5.0225188.

[6] Paul N. Patrone, Andrew Dienstfrey, Andrea R. Browning, Samuel Tucker, and Stephen Christensen. Uncertainty quantification in molecular dynamics studies of the glass transition temperature. *Polymer*, 87:246–259, March 2016. ISSN 0032-3861. doi: 10.1016/j.polymer.2016.01.074. URL https://www.sciencedirect.com/science/article/pii/S003238611630074X.